Embedding of atoms into the nanopore sites of the C_6N_6 and C_6N_8 porous carbon nitride monolayers with tunable electronic properties

Reference:

Bafekry Asadollah, Stampfl Catherine, Akgenc Berna, Mortazavi Bohayra, Ghergherehchi Mitra, Nguyen Ch. V..- Embedding of atoms into the nanopore sites of the C_6N_6 and C_6N_8 porous carbon nitride monolayers with tunable electronic properties
Physical chemistry, chemical physics / Royal Society of Chemistry [London] - ISSN 1463-9076 - 22:11(2020), p. 6418-6433
Full text (Publisher's DOI): https://doi.org/10.1039/D0CP00093K
To cite this reference: https://hdl.handle.net/10067/1686170151162165141

View Article Online
View Journal

PCCP

Physical Chemistry Chemical Physics

Accepted Manuscript

This article can be cited before page numbers have been issued, to do this please use: A. Bafekry, C. Stampfl, B. Akgenc, B. Mortazavi, M. Ghergherehchi and C. V. Nguyen, *Phys. Chem. Chem. Phys.*, 2020, DOI: 10.1039/D0CP00093K.

ROYAL SOCIETY
OF CHEMISTRY

rsc.li/pccp

View Article Online
DOI: 10.1039/D0CP00093K

Embedding of atoms into the holey site of the C_6N_6 and C_6N_8 porous carbon nitride monolayers with tunable electronic properties

Asadollah Bafekry,[*,†] Catherine Stampfl,[¶] Berna Akgenc,[§] Bohayra Mortazavi,[‖]
Mitra Ghergherehchi,[*,#] and Ch. V. Nguyen[@]

†*Department of Physics, University of Guilan, 41335-1914, Rasht, Iran*

‡*Department of Physics, University of Antwerp, Groenenborgerlaan 171, B-2020 Antwerp, Belgium.*

¶*School of Physics, The University of Sydney, New South Wales 2006, Australia*

§*Department of Physics, Kirklareli University, Kirklareli, Turkey*

‖*Institute of Continuum Mechanics, Leibniz Universitat Hannover, Appelstrabe 11, 30157 Hannover, Germany*

⊥*Cluster of Excellence PhoenixD (Photonics, Optics, and Engineering-Innovation Across Disciplines), Gottfried Wilhelm Leibniz Universitat Hannover, Hannover, Germany*

#*College of Electronic and Electrical Engineering, Sungkyun kwan University, Suwon, Korea*

@*Department of Materials Science and Engineering, Le Quy Don Technical University, Hanoi, Vietnam*

E-mail: Bafekry.asad@gmail.com; mitragh@skku.edu

Abstract

Using first-principles calculations, we study affect of various embedding atoms into

View Article Online
DOI: 10.1039/D0CP00093K

holey site of both C_6N_6 and C_6N_8 monolayers. Our results indicate that embedding atom significantly affects electronic and magnetic properties of C_6N_6 and C_6N_8 monolayers and lead to extraordinary and multifarious electronic properties, such as metallic, half-metallic, spin-glass semiconductor and dilute-magnetic semiconductor. Our results reveal that H atom concentration dramatically affects to C_6N_6 monolayer. While increasing H coverage, the impurity states also increase due to H atoms around Fermi-level. C_6N_6 shows metallic character when H atom concentration reaches to 6.25%. Moreover, charging effect on the electronic properties of both Cr@C_6N_6 and C@C_6N_8 is also studied. Cr@C_6N_6 is a ferromagnetic-metal with a magnetic moment of 2.40 μ_B, and when 0.2 electron is added and removed, it is remain a ferromagnetic-metal with magnetic moment of 2.57 and 2.77 μ_B, respectively. Interestingly, one can observe a semi-metal, where the VBM and CBM in the both of spin channels, touch each other near Fermi-level. The C@C_6N_8 is a semiconductor with a nontrivial band gap. When 0.2 electron is removed, it remains metallic and under excess electronic charge exhibit a half-metallic.

Introduction

Recently, two-dimensional carbon nitride (2D-CN) nanomaterials have attracted remarkable attention due to their astonishing experimental advances concerning their synthesis. 2D-CN have rapidly revealed as one of the hottest topic in physics, chemistry and material science.[1–3] They have been suggested as promising candidates for various advanced applications such as nanoelectronics, energy storage and catalysis.[4–13] 2D-CN monolayers and their belong to 2D allotropes can be identified with general formula of C_xN_y (x : number of C atoms, y : number of N atoms), and they can be produced by multifarious chemistry process such as evaporation, calcination method, etc. 2D-CN allotropes show various electronic properties, ranging from semiconducting to half-metallic depending on the composition of C and N atoms in the atomic lattice. 2D-CN monolayers exhibit various electronic, mechanical properties

View Article Online
DOI: 10.1039/D0CP00093K

and thermal conductivity,[14,15] originating from their unique atomic lattices formed by strong covalent bonds.[16–19] Successfully synthesized two-layered CN monolayers (C_2N, C_3N, C_6N_8 and C_6N_6) using a bottom-up chemical reaction have motivated researchers to consider possible attractive nanosheets for tuning the band gap engineering.[16,20–22] Although some 2D-CN nanosheets can be experimentally produced by different chemical approaches, some of them have been just theoretically examined up to date.[23–27] For instance, C_6N_6 is the one of the 2D-CN allotropes which have two hexagonal rings linked by C-C bonds have been theoretically investigated.[1,28–30] Recent theoretical work showed that C_6N_6 exhibits topologically nontrivial band gap, which can be modulated to a topological insulator by doping.[1]

There have been several efforts to seeking suitable spintronic material such as Dilute-magnetic semiconductors (DMS). For the reason, first principle calculations based on density functional theory have been performed for transition-metal (TM) atoms embedded in semiconductor 2D carbon nitride monolayers.[2,31–34] The nature of semiconductor behavior and band alignment of these 2D-CN nanosheets are also found to be ideal material for hydrogen production by photocatalytic water splitting.[35–37] Theoretical studies by a ruby model have showed that electronic states near the Fermi level are topologically nontrivial.[38] 2D-CN with a stoichiometry of C_6N_8, which building blocks are jointed together directly or sp^2-hybridized nitrogen/carbon atoms, have been synthesized very recently.[10,20,39–41] After synthesis of C_6N_8, the electronic and magnetic properties have been studied in detail.[42,43] The results demonstrate that C_6N_8 is not a magnetic material, it shows intrinsic half-metallicity when replacing a nitrogen atom with a carbon atom.[3] Recently, is shown that the photoactivity of C_6N_8 carbon nitride allotrope can be enhanced via nonmetal atom doping and it is obtained that C 6 N 8 membrane has high capability to separate helium from gas molecules.[44,45] Researchers have proposed several new types of carbon nitride membranes by theoretical calculations, and some of these membranes have already been synthesized, but among them mostly interested ones are C_6N_6 and C_6N_8 monolayers.[1,46]

View Article Online
DOI: 10.1039/D0CP00093K

Over the past decade, tunable electronic and magnetic engineering of two-dimensional (2D) materials have drawn extraordinary attention due to its excellent properties. In this view, several ideas such as introducing defect, applying electric fields and strain engineering, functionalization, and impurities atom have been produced to tunable electronic and magnetic properties of carbon nitride monolayers.

In this study, we systematically analyzed the effect of impurity atom doping as H, O, S, F, Cl, B, C, N, Si, P, Li, Na, K, Be, Mg, Ca, Al, Sc, Ti, V, Cr, Mn, Fe, Co, Ni and Zn into the holey site both of C_6N_6 and C_6N_8 monolayers using first-principles calculations. Our results confirm that the electronic and magnetic properties can be tuned by different embedding atoms and they significantly affect by the concentration of H atom. Next, the electronic and magnetic properties show various electronic characteristics from metallic to semiconductor, and induce magnetism in C_6N_6. The magnetic moment can be modulated and transition from semiconductor to metal can be achieved by applying of charging and strain. Furthermore, our results demonstrate that a number of effective possibilities can be tune the electronic and magnetic properties both of C_6N_6 and C_6N_8 monolayers.

Method

Density functional theory based calculations were performed the generalized gradient approximation for the exchange-correlation functional as proposed by Perdew-Burke-Ernzerhof (GGA-PBE),[87] along with norm-conserving pseudopotentials[88] as implemented in OpenMX package. The plane-wave basis set was taken as energy cutoff of 350 Ry. The wave functions are developed with the linear combination of multiple pseudoatomic orbitals (LCPAOs) which is suitable for large-scale electronic properties.[89,90] The integration in the **k**-point mesh was performed using $23 \times 23 \times 1$ Monkhorst-Pack scheme for the primitive unit cell and scaled according to the size of supercells.[91] 2D-CN was modeled with vacuum region more than 20 Å to avoid interaction between neighboring slabs. The ground state structures was obtained

View Article Online
DOI: 10.1039/D0CP00093K

by using a quasi-Newton algorithm. The ground state geometric structures were relaxed until the residual forces on the atoms became smaller than 1 meV/Å. The scanning tunneling microscopy (STM) images are obtained by the Tersoff-Hamann theory that based on OpenMX package.[92] WSxM software was used as post-process tool to plot STM simulated images, which assume a bias of +2.0 V.[93] The charge transfer analyses were performed by using the Mulliken charge analysis.[94]

Results

Pristine C_6N_6 and C_6N_8 monolayers

2D-CN can be formed in many allotropes because of its ability to exist in different hybridization. In this study, we have explored C_6N_6 and C_6N_8 monolayers. We have started with get to their optimized geometric structures as shown in Fig. 1(a). The lattice constant of the optimized C_6N_6 is calculated to be 7.11 Å. The bond distances of C-C and C-H are found 1.503 Å and 1.343 Å, respectively. The diameter of the nanopore is 5.447 Å, which is equivalent to the distance from one N atom to the opposite N atom across the nanopore; in addition the lattice is completely planar which are consistent with previous reports.[30,95–97] The dynamical stability of C_6N_6 and C_6N_8 monolayers by phonon spectrum has also been determined from first-principles calculations in previous reports.[98,99]

The lattice constant of C_6N_8 is also found 7.14 Å, and there are two inequivalent C-N bond lenghts with values of 1.414 and 1.455 Å. Due to the C-N-C angle is equal to 120° and N-C-N angles are 118° and 122°, the ring of C_6N_8 is not a regular hexagon. It can be seen that every six C-N hexagon rings enclose a nanopore, while the edges are surrounded by six N atoms with nanopore diameter of 4.773 Å (see Fig. 1(a)), which are agreement with previous reports.[33,95,100?] The total charge density and charge density difference plots of C_6N_6 and C_6N_8 are provided in Fig. 1(a), where yellow and blue regions indicate that depletion and accumulation, respectively. According to the charge density difference plots, N atoms are negatively charged, while each C atom is positively charged. The N atom has a larger electro-negativity (C is 2.55 and N is 3.04), explaining the greater electron density at the N atoms, when Pauling scale electro-negativity is taken account. The simulated STM images are shown in Fig. 1(b), where they are overlapped with the atomic structure. From the predicted STM images, it is easy to recognize and correlate them with the corresponding atomistic structure, in addition, the atoms around the C atom sites exhibit the bright spots.

The electronic properties of C_6N_6 and C_6N_8 are investigated by analyzing the band structure, density of states (DOS) and partial density of states (PDOS) as shown in Figs. 1(c,d). It is found that C_6N_6 monolayer is a semiconductor with a direct band gap, showing the value 1.5 eV located at the K-point (see Fig. 1(c)). This result agrees with a previous report.[30] The electronic properties of C_6N_8 demonstrates indirect semiconductor behaviour with a band gap of 1.22 eV, which is agreement with previous results.[101] From the DOS and PDOS results, we found sharp peaks (flat shallow bands) within $+2eV$ below E_F suggesting rather localized wave functions in C_6N_6 formed from the N-$s, p_{x,y}$ orbitals (see Fig. 1(d)). At the VBM, N atoms form an sp^2 configuration and lone pairs which is exhibited in the up-going band structure from the Γ to K point near E_F. The lone pairs of N-$s, p_{x,y}$ lie in in-plane orbitals, suggesting the donor nature of the nanopore, although the N/C-p_z anti-bonding delocalized orbitals form the CBM above E_F, showing the acceptor nature of C_6N_6 (see Fig. 1(d)). The filling of all the in-plane bonding orbitals imply the high stability of the C_6N_6 structure. The VBM is determined by the N-$s, p_{x,y}$ orbitals, however the CBM originates from the N/C-p_z orbitals from the results of PDOS of C_6N_8 (see Fig. 1(d)). Furthermore, we have investigated that the effect of embedding atom on the structural and electronic properties of C_6N_6 and C_6N_8 in detailed. The schematic model structure for embedding atoms into the holey site of C_6N_6 (left) and C_6N_8 (right) monolayers are shown in Fig. 2. Hereafter, the embedding atom into the holey site of the C_6N_6 or C_6N_8 monolayers, are labeled as atom@C_6N_6 or @C_6N_8, for instance, embedding H atom into the holey site of

View Article Online
DOI: 10.1039/D0CP00093K

C_6N_6 is labeled as H@C_6N_6.

Embedding of atoms into the holey site of the C_6N_6 monolayer

The optimized atomic structures of embedding H, O, S, F, Cl, B, C, N, Si, P, Li, Na, K, Be, Mg, Ca, Al, Sc, Ti, V, Cr, Mn, Fe, Co, Ni and Zn atoms into the holey site of C_6N_6, respectively, are shown in Fig. 3. The atoms interact through sp^2-hybridization and form one (for H, O, F and Cl), two (for S, B, C, Si, N and P) σ bonds to neighboring N atoms of C_6N_6. The bond lengths are found as 1.391-1.418 Å for the H, O, F and Cl atoms, respectively. The bond lengths vary from 1.417 (Si) to 1.445 (B) Å for the S, B, C, Si, N and P atoms, respectively (see Table I). We can see that upon the embedding of these atoms, the planar structure of the C_6N_6 surface is preserved, except for the F atom which induces a structural deformation along the direction perpendicular to the surface (see Fig. 3). The Li, Be and Mg atoms interact through sp^2-hybridization and form two σ bonds, whereas the Na, K and Ca atoms form six σ bonds with neighboring N atoms. Due to weaker interaction with C_6N_6, the Li, Na, K, Be, Mg and Ca atoms yield no significant distortion and only induce local deformations. The bond lengths of Na, K and Ca atoms with nearest N atoms are found as 1.626-2.674 Å (see Fig. 3 and Table I). These bond number and lengths reflect the sizes of atoms. The TMs atoms bind to the two nearest N atom of C_6N_6 and the bond lengths are in the range of 1.853-2.200 Å (see Fig. 3 and Table I). It is found that notably larger than the 1.445 and 1.428 Å for the C-C and C-N bond lengths of pristine C_6N_6 as expected.

The calculation of electronic structures of embedding atom@C_6N_6 are presented in Fig. 4. The electronic properties are calculated with spin-polarized case and ↑ and ↓ spin channels represented with blue-lines and red-dashed lines, respectively. Our results show that the band structures of embedding atom@C_6N_6 are altered and give rise to localized states in the fundamental band gap when compare with pristine C_6N_6. The H, F, Cl, B, N, P and

DOI: 10.1039/D0CP00093K

Al@C_6N_6 structure exhibits a dilute-magnetic semiconductor (DM-SC) character and degenerates in the ↑ ↓ spin channels are broken and induce magnetic moment in the range of 1-4 μ_B. The O, S, C, Si, K and Be@C_6N_6 structures are indirect semiconductor behavior with a band gap as large as 1 eV, where the VBM and CBM are located at K and M points, respectively. Our results show that Mg@C_6N_6 is a direct semiconductor with a narrow band gap of 0.1 eV with the VBM and CBM located at Γ point. The Li, Na and Ca@C_6N_6 structures are metallic with no spin polarized states. Interestingly, the Ca@C_6N_6 exhibit a negligible band gap of about 3 meV at the Γ point. The embedding TM atoms such as Sc and Mn atoms results in half-metallic electronic structure and trigger magnetic moments of 0.80 and 3.00 $\mu_{\rm B}$, respectively. The systems Ti, V and Co@C_6N_6 become a spin-gapless semiconductor with magnetic moments of 1.90, 2.76 and 1.00 μ_B, respectively. More clearly, spin gapless (semiconducting) is called upon the ↑ (↓) spin channels and the VBM of the ↓ spin channel touches the E_F at that circumstance. The half-metals and spin-gapless semiconductors are expected to open up many prospects for device applications, such as spin filters, spin diodes, spin valves, and spin photo-conductor. The Fe@C_6N_6 system exhibits a DM-SC character and degenerates in the ↑ and ↓ spin channels of electrons are lifted with a magnetic moment of 2 μ_B. In addition, Cu@C_6N_6 shows ferromagnetic-metal behavior and induces magnetic moment of 0.5 μ_B. The Ni and Zn@C_6N_6 systems show semiconductor behavior with direct band gaps of 0.9 and 1.0 eV, respectively. In this situation, the VBM and CBM are located at the K and Γ points, respectively.

The DOS and PDOS results of embedding atom@C_6N_6 are given as Fig. 5. PDOS of O@C_6N_6 have showed that the states around E_F arise from O-$p_{x,y,z}$(↓) and N/C-p_z(↑) orbital. The metallic states of Li, Na and K@C_6N_8 with the impurity levels crossing E_F mainly stemming from the C/N-$p_{x,y}$ orbitals around E_F. Though the 3d-orbitals shell of the TMs atoms are partially occupied, 3d and 4s-orbital states of the TMs atoms have similar energy values. The initial magnetic moment of isolated TMs atoms are nonzero in circumstance of 3d-orbitals shell is completely occupied. Due to the 3d-orbitals of the TM

View Article Online
DOI: 10.1039/D0CP00093K

atoms are partially occupied, the embedded atom@C_6N_6s show various electronic properties. The strong hybridization and covalent bonding character between 3d-orbitals for TM atoms and the C/N-p_z orbital states of C_6N_6 is monitored from PDOS calculations. The half-metallic state of Fe and Co@C_6N_6 comes from Fe/Co-$d_{yz,xz}/d_{xy,x^2-y^2}$ and N/C-p_z orbital states in the (↑) spin channel. In the same time, the ferromagntic-metallic state of Cr and Cu@C_6N_6 stemming from bands around E_F and N/C-p_z(↑) orbital states. The VBM of Ni@C_6N_6 mainly originates from the hybridization of Ni-$d_{yz,xz}/s$ with C/N-p_z orbitals, while the CBM comes from hybridization with C/N-p_z (↑).

Embedding of atom into the holey site of the C_6N_8 monolayer

The optimized atomic structures of embedding H, O, S, F, Cl, B, C, Si, N, and P atoms into the holey site of @C_6N_8 are shown in Fig. 6, respectively. We found that upon the embedding of these atoms, the planar structure of C_6N_8 is not maintained. The embedded O atom interacts through sp^2-hybridization and form one σ bond to the N atom of C_6N_8, while the S, Cl, B, S, Si, N and P atoms form two σ bonds to neighboring N atoms of C_6N_8. The calculated bond length of O atom is found as 1.297 Å and induces a structural deformation along the surface normal of C_6N_8. According to our results, S, B, C, Si, N and P atoms interact through sp^2-hybridization and form two σ bonds, where the bond lengths are calculated to range from 1.396 Å (C) to 2.180 (Cl) Å (see Table I). We can see that the O, F and B atoms induce some structural distortion on the surface of C_6N_8 as shown in Fig. 6.

Neighboring N atoms form two for Be, four for Li and Mg, six for Na, K and C σ bonds with embedding Li, Na, K, Be, Mg and Ca atoms and their bond lengths to the nearest N atoms are in the range of 1.441 and 2.429 Å. Our results show that TM atoms bond to the N host atom of C_6N_8 and form tree for Fe, Co, Ni and Cu, four for Mn and Zn and six for

View Article Online
DOI: 10.1039/D0CP00093K

Sc, V and Cr σ bonds. These results show strong distortions of planar structure upon the embedding Mn, Fe, Co, Cu and Zn atoms. The calculated bond lengths of TMs atoms to nearest N atoms range from 1.808 Å for Fe to 2.335 for Zn Å (see Table I).

The electronic structure of H, O, S, F, Cl, B, C, Si, N, and P atoms embedded C_6N_8 is demonstrated in Fig. 7. The embedded F, B and Al@C_6N_8 shows dilute-magnetic semiconductor behaviour with magnetic moments of 1.10 and 0.85 μ_B, respectively. The ↑ spin channels of Cl, N, P, Li, Na and K@C_6N_8 shows a metallic character, while the ↓ spin channels show semiconductor character, whereas for Sc@C_6N_8, it is vice versa, the systems become half-metals. For the O, S, Be and Zn@C_6N_8 structures, the situation was quite different; direct semiconductor with band gaps of 1.4, 0.5, 0.4 and 1.5 eV respectively, are shown. The VBM and CBM are located at the Γ point at this circumstance. Where the VBM and CBM are located at the M point, interestingly, the C@C_6N_8 becomes a direct semiconductor with a 25 meV narrow band gap. The Mg and Sc@C_6N_8 monolayers turn into a metal, whereas the H and Al@C_6N_8 systems show a spin-gapless semiconductor character. With the embedding of Si, Ca, Ti, Fe and Co atoms into C_6N_8, the system becomes a ferromagnetic-metal with the impurity levels crossing E_F and magnetic moments of 0.3, 1.1, 1.6, 1.68 and 0.75 μ_B are induced, respectively. The V, Cr, Mn, Co and Ni@C_6N_8 structures become half-metals and magnetic moments of about 1.97-3.00 μ_B are induced, where the band gaps in the ↑ spin channel are in the range of 0.45 (Ni)-1.4 eV (Mn). The acquired results indicate that findings are interesting because different and contrasting electronic behavior can be formed depending on the type of embedding atom.

The DOS and PDOS results of embedding atom@C_6N_8 are given in supplementary information (SI) Fig. S1. DOS and PDOS calculations of embedding atom@C_6N_8 show that there is obviously asymmetry spin splitting around the E_F in ↑ and ↓ spin states, implying magnetic properties. Because of the hybridization of the p_z-orbital of the embedded atoms with C/N-p_z orbitals of the nearest atoms, the impurity states are around E_F in the case of S, B, C, Si, N, and P@C_6N_8. The DOS of Li, Na, K, Be, Mg, Ca, and Al@C_6N_8 are different from that of pristine C_6N_8, exhibiting an impurity state around E_F. According to PDOS calculations, the impurity states mainly come from the N/C-p_z states. The magnetic state results are found for the Li, Na, K, Be, Ca and Al@C_6N_8 structures. The PDOS result of Mg@C_6N_8 show the semiconductor to metal transition due to interaction with the Mg atom and the N atoms of C_6N_8. We also found metallic behavior in the ↑ spin channel of Ti@C_6N_8 originate from the $s, d_{yz,xz}$-orbitals, while the half-metallic character of Cr@C_6N_8 is mainly from the $d_{xy,yz,xz}/d_{x^2-y^2}$ (↑) orbitals. The PDOS of Mn@C_6N_8 indicates that the VBM originates from $d_{xy}/d_{x^2-y^2}$ (↑), while the CBM arises from $d_{yz,xz}/d_{z^2}$ ↓ orbitals. The Co@C_6N_8 system becomes a ferromagnetic-metal with the impurity level crossing E_F and induces magnetic moment of 0.75 μ_B. The metallic band originates from Co-$d_{yz,xz}$ (↑) with C-$p_{x,y}$ (↑) orbital states as seen in Fig. S1. The spin-splitting can be found around the E_F due to 3d-orbital peaks in ↑ and ↓ spin channels in the case of Sc, V, Fe and Zn@C_6N_8. This metallic bands originate from the $d_{xy,yz,xz}/d_{z^2}$ and N-p_z states in both spin channels.

The Fig. 8 presents the difference charge densities with bond formation, charge accumulation, and depletion regions. The O and F atoms form chemical bonds, and there is electron depletion on C_6N_6, while electron accumulation on the embedded atoms, i.e. there is charge transfers from C_6N_6 to O (0.33 e) and F (0.24 e) atoms (see Table I). Furthermore, in the other atoms we find an electron accumulation on C_6N_6, while electrons are depleted on the embedded atoms, thus there is charge transfers from the embedded atoms to C_6N_6. The difference charge density of atom-embedded C_6N_8 are shown in Fig. 8(b). We can see that electrons are depleted on the atoms of C_6N_8, while the majority of electron accumulation is on the C and P, atoms, i.e. there is charge transfers from C (0.42 e) and P (0.48 e) atoms to C_6N_8. Depending on the type of embedded atoms can be effectively tuned their electronic properties. Hereby, we can achieve a metal, ferromagnetic-metal, half-metal, DM-SC, SG-SC in these monolayers. The spin density difference of the embedding atom@$C_6N_{6,8}$ structures are shown in Figs. 9(a,b). It can observed that the spin mainly accumulates around atoms embedded and N neighbors, thus displaying a ferromagnetic interaction (H, F, Co and Cu)

View Article Online
DOI: 10.1039/D0CP00093K

between them. While for the Ti, Cr and Mn@C_6N_6 systems, a highly localized difference spin density around Ti, Cr and Mn atoms and the three N neighbors can be observed, thus indicating an anti-ferromagnetic interaction between them.

Effect of H atom concentration

Next, we continued to investigate the structural and electronic properties of H@C_6N_6 as a function of the H atom coverage. We have reveal that H atom coverage induces metallic character, which can be continuously tuned by varying the concentration from 3.1% (1 H) to 12.5% (6 H). The optimized structures of H@C_6N_6 for the various concentrations are shown in the top of Fig. 10. Increasing coverage affects its atomic structure of C_6N_6 as compared to pristine C_6N_6. For 3.1% concentration of H@C_6N_6, the nearest N atom moves in the upward direction as seen in Fig. 10. The surface distortion becomes more apparent and the bond length dramatically changes when the H atom ratio increases up to 10.4%. The coverage eventually reaches to 12.5 %, similar behavior is observed with the surface becoming more distorted. The electronic band structure of H@C_6N_6 as a function of concentration is shown in Fig. 10. The optimized structures is shown in the top of panel.

We have demonstrated that the band structure of C_6N_6 dramatically modify by H atom coverage and shows diverse electronic behavior. For instance; a dilute-magnetic semiconductor behaviour is obtained at 3.1% concentration, while an indirect semiconductor with a band gap of 1 eV is obtained at 4.16% concentration, where VBM and CBM are located at the K and M points, respectively. With increasing H coverage, the impurity states increase stemming from the H atoms around Fermi-level. Notice that, in the 6.25% concentration, system exhibits a metallic character and for other concentrations, C_6N_6 monolayer is semiconductor.

View Article Online
DOI: 10.1039/D0CP00093K

Effect of charging

We finally shift our attention to the effect of charging, applying an electric field and strain on the electronic properties of C and Cr embedded atom both C_6N_6 and C_6N_8 monolayers. The electronic structures of the Cr and C@$C_6N_{6,8}$ structures as a function of charging are investigated as seen in Figs. 11(a,b). Cr@C_6N_6 shows ferromagnetic-metallic behavior with a magnetic moment of 2.40 μ_B. When applying q = +0.5 charging, the magnetic moment increases to 2.57 μ_B and its electronic property remains as ferromagnetic-metal. In the other scenario, while excising electronic charge of q = -0.2 e, the magnetic moment increases to 2.77 μ_B. In this case its electronic property changes metallic in one spin channel, and a semiconductor in the other channel, which result as electron transport only allows in one spin channel. Interestingly, one can observe a nodal-line, where the VBM and CBM in the ↑ and ↓ spin channels, touch each other near E_F. The C@C_6N_8 is a semiconductor with a nontrivial band gap. When 0.2 electron is removed (q = -0.2 e) it remains metallic. Half-metallic behavior with an induced magnetic moment of 0.2 μ_B for q = +0.2 e results under excess electronic charge a reverse situation.

Conclusion

In the present study the effects of embedding atoms on the structural, electronic, and magnetic properties both of C_6N_6 and C_6N_8 monolayers are explored by first-principles calculations. Our theoretical results have revealed that both of pristine C_6N_6 and (C_6N_8) monolayers are semiconductor and they show various electronic character depending on the type of embedded atoms, including; metal with Li, Na, K and Ca (Mg and Sc); half-metallic with Si, Sc, Mn, Fe, and Co (Cl, N, P, Li, Na, K, Sc, V, Cr, Mn, Co and Ni); ferromagnetic-metal with Cu (Si, Ca, Ti, Fe and Co); semiconductor with for O, C, Be, Mg, Ni and Zn (O, S, C, Be and Zn); dilute-magnetic semiconductor with H, S, F, Cl, B, C, N, P, Al and Cr (F, B and Cu) and spin-gapless semiconductor with Ti and V (H and Al).

View Article Online
DOI: 10.1039/D0CP00093K

In addition, we have observed that the electronic and magnetic properties can be effectively modified by the concentration of H atoms embedded in C_6N_6. We showed that dilute-magnetic semiconductor and semiconductor behavior for 3.1% and 4.16% concentration, respectively. With increasing H coverage, the impurity states stemming from the H atoms around Fermi-level increase and in concentration of 6.25%, exhibit a metallic character. Moreover, we have explored the effect of charging on the electronic properties for Cr and C atoms@$C_6N_{6,8}$. Our results showed that Cr@C_6N_6 is a ferromagnetic-metal with a magnetic moment of 2.40 μ_B. The magnetic moment increases to 2.57 μ_B when 0.2 electron is added and remains a ferromagnetic-metal, while for an excess electronic charge when 0.2 electron is removed, the magnetic moment increases to 2.77 μ_B. The C@C_6N_8 is found as semiconductor with a band gap. When 0.2 electron is removed it remains metallic and under excess electronic charge a reverse situation is observed, where a half-metallic behavior results with an induced magnetic moment of 0.2 μ_B when 0.2 electron is added.

Conflicts of interest

The authors declare that there are no conflicts of interest regarding the publication of this paper.

ACKNOWLEDGMENTS

This work was supported by the National Research Foundation of Korea(NRF) grant funded by the Korea government(MSIT)(NRF-2017R1A2B2011989). B. M. appreciates the funding by the Deutsche Forschungsgemeinschaft (DFG, German Research Foundation) under Germany's Excellence Strategy within the Cluster of Excellence PhoenixD (EXC 2122, Project ID 390833453).

View Article Online
DOI: 10.1039/D0CP00093K

References

(1) Wang, A.; Zhang, X.; Zhao, M. Topological insulator states in a honeycomb lattice of s-triazines. *Nanoscale* **2014**, *6*, 11157–11162.

(2) Abdullahi, Y. Z.; Yoon, T. L.; Halim, M. M.; Hashim, M. R.; Lim, T. L. Mechanical and electronic properties of graphitic carbon nitride sheet: First-principles calculations. *Solid State Communications* **2016**, *248*, 144 – 150.

(3) Du, A.; Sanvito, S.; Smith, S. C. First-Principles Prediction of Metal-Free Magnetism and Intrinsic Half-Metallicity in Graphitic Carbon Nitride. *Phys. Rev. Lett.* **2012**, *108*, 197207.

(4) Zhao, X.; Pan, D.; Chen, X.; Li, R.; Jiang, T.; Wang, W.; Li, G.; Leung, D. Y. g-C_3N_4 photoanode for photoelectrocatalytic synergistic pollutant degradation and hydrogen evolution. *Applied Surface Science* **2019**, *467-468*, 658 – 665.

(5) Guo, G.-C.; Wang, R.-Z.; Ming, B.-M.; Wang, C.; Luo, S.-W.; Lai, C.; Zhang, M. Trap effects on vacancy defect of C_3N as anode material in Li-ion battery. *Appl. Surf. Sci.* **2019**, *475*, 102 – 108.

(6) Gao, X.; Shen, Y.; Ma, Y.; Wu, S.; Zhou, Z. First-principles insights into efficient band gap engineering of the blue phosphorus/g-C_3N bilayer heterostructure via an external vertical strain. *Appl. Surf. Sci.* **2019**, *479*, 1098 – 1104.

(7) Yong, Y.; Cui, H.; Zhou, Q.; Su, X.; Kuang, Y.; Li, X. C_2N monolayer as NH_3 and NO sensors: A DFT study. *Appl. Surf. Sci.* **2019**, *487*, 488 – 495.

(8) Shi, L.-B.; Yang, M.; Cao, S.; You, Q.; Niu, Y.-Y.; Wang, Y.-Z. Elastic behavior and intrinsic carrier mobility for monolayer SnS and SnSe: First-principles calculations. *App. Surf. Sci.* **2019**, *492*, 435 – 448.

View Article Online
DOI: 10.1039/D0CP00093K

(9) Hua, W. Q.; Kourosh, K.-Z.; Andras, K.; N., C. J.; S., S. M. Electronics and optoelectronics of two-dimensional transition metal dichalcogenides. *Nat. Nanotech.* **2012**, *7*, 699.

(10) Li, X.-H.; Wang, X.; Antonietti, M. Mesoporous g-C_3N_4 nanorods as multifunctional supports of ultrafine metal nanoparticles: hydrogen generation from water and reduction of nitrophenol with tandem catalysis in one step. *Chem. Sci.* **2012**, *3*, 2170–2174.

(11) Zhang, J.; Grzelczak, M.; Hou, Y.; Maeda, K.; Domen, K.; Fu, X.; Antonietti, M.; Wang, X. Photocatalytic oxidation of water by polymeric carbon nitride nanohybrids made of sustainable elements. *Chem. Sci.* **2012**, *3*, 443–446.

(12) Zhang, X.; Xie, X.; Wang, H.; Zhang, J.; Pan, B.; Xie, Y. Enhanced Photoresponsive Ultrathin Graphitic-Phase C_3N_4 Nanosheets for Bioimaging. *Journal of the American Chemical Society* **2013**, *135*, 18–21.

(13) Zhang, X.; Wang, H.; Wang, H.; Zhang, Q.; Xie, J.; Tian, Y.; Wang, J.; Xie, Y. Single-Layered Graphitic-C_3N_4 Quantum Dots for Two-Photon Fluorescence Imaging of Cellular Nucleus. *Adv. Mater.* **2014**, *26*, 4438–4443.

(14) Mortazavi, B. Ultra high stiffness and thermal conductivity of graphene like C_3N. *Carbon* **2017**, *118*, 25 – 34.

(15) Mortazavi, B.; Cuniberti, G.; Rabczuk, T. Mechanical properties and thermal conductivity of graphitic carbon nitride: A molecular dynamics study. *Computational Materials Science* **2015**, *99*, 285 – 289.

(16) Zhou, Q.; Wu, M.; Zhang, M.; Xu, G.; Yao, B.; Li, C.; Shi, G. Graphene-based electrochemical capacitors with integrated high-performance. *Materials Today Energy* **2017**, *6*, 181 – 188.

View Article Online
DOI: 10.1039/D0CP00093K

(17) Lee, S. U.; Belosludov, R. V.; Mizuseki, H.; Kawazoe, Y. Designing Nanogadgetry for Nanoelectronic Devices with Nitrogen-Doped Capped Carbon Nanotubes. *Small* **2009**, *5*, 1769–1775.

(18) Li, J.; Cui, W.; Sun, Y.; Chu, Y.; Cen, W.; Dong, F. Directional electron delivery via a vertical channel between g-C_3N_4 layers promotes photocatalytic efficiency. *J. Mater. Chem. A* **2017**, *5*, 9358–9364.

(19) Zheng, Y.; Liu, J.; Liang, J.; Jaroniec, M.; Qiao, S. Z. Graphitic carbon nitride materials: controllable synthesis and applications in fuel cells and photocatalysis. *Energy Environ. Sci.* **2012**, *5*, 6717–6731.

(20) Thomas, A.; Fischer, A.; Goettmann, F.; Antonietti, M.; Muller, J.-O.; Schlogl, R.; Carlsson, J. M. Graphitic carbon nitride materials: variation of structure and morphology and their use as metal-free catalysts. *J. Mater. Chem.* **2008**, *18*, 4893–4908.

(21) Algara-Siller, G.; Severin, N.; Chong, S. Y.; Bjorkman, T.; Palgrave, R. G.; Laybourn, A.; Antonietti, M.; Khimyak, Y. Z.; Krasheninnikov, A. V.; Rabe, J. P.; Kaiser, U.; Cooper, A. I.; Thomas, A.; Bojdys, M. J. Triazine-Based Graphitic Carbon Nitride: a Two-Dimensional Semiconductor. *Angewandte Chemie 126*, 7580–7585.

(22) Mahmood Javeed, Lee Eun Kwang, Jung Minbok, Shin Dongbin, Jeon In-Yup, Jung Sun-Min, Choi Hyun-Jung, Seo Jeong-Min, Bae Seo-Yoon, Sohn So-Dam, Park Noejung, Oh Joon Hak, Shin Hyung-Joon, Baek Jong-Beom, Nitrogenated holey two-dimensional structures. *Nat. Commun.* **2015**, *6*, 6486.

(23) Groenewolt, M.; Antonietti, M. Synthesis of g-C_3N_4 Nanoparticles in Mesoporous Silica Host Matrices. *Advanced Materials* **2005**, *17*, 1789–1792.

(24) Lee, J. S.; Wang, X.; Luo, H.; Dai, S. Fluidic Carbon Precursors for Formation of Functional Carbon under Ambient Pressure Based on Ionic Liquids. *Advanced Materials* **2010**, *22*, 1004–1007.

View Article Online
DOI: 10.1039/D0CP00093K

(25) Xu, Y.; Gao, S.-P. Band gap of C_3N_4 in the GW approximation. *International Journal of Hydrogen Energy* **2012**, *37*, 11072 – 11080, Hydrogen Enriched Methane.

(26) Khabashesku, V. N.; Zimmerman, J. L.; Margrave, J. L. Powder Synthesis and Characterization of Amorphous Carbon Nitride. *Chemistry of Materials* **2000**, *12*, 3264–3270.

(27) Yang, B.; Zhou, H.; Zhang, X.; Zhao, M. Electron spin-polarization and band gap engineering in carbon-modified graphitic carbon nitrides. *J. Mater. Chem. C* **2015**, *3*, 10886–10891.

(28) Guo, Q.; Yang, Q.; Yi, C.; Zhu, L.; Xie, Y. Synthesis of carbon nitrides with graphite-like or onion-like lamellar structures via a solvent-free route at low temperatures. *Carbon* **2005**, *43*, 1386 – 1391.

(29) Self-assembled one-dimensional carbon nitride architectures. *Diamond and Related Materials* **2006**, *15*, 1593 – 1600.

(30) Qiu, H.; Wang, Z.; Sheng, X. First-principles prediction of an intrinsic half-metallic graphitic hydrogenated carbon nitride. *Physics Letters A* **2013**, *377*, 347 – 350.

(31) Zhang, S.; Chi, R.; Li, C.; Jia, Y. Structural, electronic and magnetic properties of 3d transition metals embedded graphene-like carbon nitride sheet: A DFT + U study. *Physics Letters A* **2016**, *380*, 1373 – 1377.

(32) Ghosh, D.; Periyasamy, G.; Pandey, B.; Pati, S. K. Computational studies on magnetism and the optical properties of transition metal embedded graphitic carbon nitride sheets. *J. Mater. Chem. C* **2014**, *2*, 7943–7951.

(33) Choudhuri, I.; Bhattacharyya, G.; Kumar, S.; Pathak, B. Metal-free half-metallicity in a high energy phase C-doped g-C_3N_4 system: a high Curie temperature planar system. *J. Mater. Chem. C* **2016**, *4*, 11530–11539.

View Article Online
DOI: 10.1039/D0CP00093K

(34) Choudhuri, I.; Garg, P.; Pathak, B. TM@gt-C_3N_4 monolayers: high-temperature ferromagnetism and high anisotropy. *J. Mater. Chem. C* **2016**, *4*, 8253–8262.

(35) Jiang, X.; Wang, P.; Zhao, J. 2D covalent triazine framework: a new class of organic photocatalyst for water splitting. *J. Mater. Chem. A* **2015**, *3*, 7750–7758.

(36) Qu Yuanyuan,; Li Feng,; Zhou Hongcai,; Zhao Mingwen, Highly Efficient Quantum Sieving in Porous Graphene-like Carbon Nitride for Light Isotopes Separation. *Sci. Rep.* **2016**, *6*, 19952.

(37) Siwei, Y.; Wei, L.; Caichao, Y.; Gang, W.; He, T.; Chong, Z.; Peng, H.; Guqiao, D.; Xiaoming, X.; Yang, L.; Yeshayahu, L.; ShuitâĂŘTong, L.; Zhenhui, K.; Mianheng, J. C_3N-A 2D Crystalline, Hole-Free, Tunable-NarrowâĂŘBandgap Semiconductor with Ferromagnetic Properties. *Adv. Mater.* **2016**, *29*, 1605625.

(38) Li, H.; Hu, H.; Bao, C.; Hua, J.; Zhou, H.; Liu, X.; Liu, X.; Zhao, M. Tensile strain induced half-metallicity in graphene-like carbon nitride. *Phys. Chem. Chem. Phys.* **2015**, *17*, 6028–6035.

(39) Kroke, E.; Schwarz, M.; Horath-Bordon, E.; Kroll, P.; Noll, B.; Norman, A. D. Tri-s-triazine derivatives. Part I. From trichloro-tri-s-triazine to graphitic C_3N_4 structures. *New J. Chem.* **2002**, *26*, 508–512.

(40) Jurgens, B.; Irran, E.; Senker, J.; Kroll, P.; MÃijller, H.; Schnick, W. Melem (2,5,8-Triamino-tri-s-triazine), an Important Intermediate during Condensation of Melamine Rings to Graphitic Carbon Nitride:âĂĽ Synthesis, Structure Determination by X-ray Powder Diffractometry, Solid-State NMR, and Theoretical Studies. *Journal of the American Chemical Society* **2003**, *125*, 10288–10300.

(41) Sehnert, J.; Baerwinkel, K.; Senker, J. Ab Initio Calculation of Solid-State NMR Spectra for Different Triazine and Heptazine Based Structure Proposals of g-C_3N_4. *The Journal of Physical Chemistry B* **2007**, *111*, 10671–10680.

View Article Online
DOI: 10.1039/D0CP00093K

(42) Hart, J. N.; Claeyssens, F.; Allan, N. L.; May, P. W. Carbon nitride: Ab initio investigation of carbon-rich phases. *Phys. Rev. B* **2009**, *80*, 174111.

(43) Snis, A.; Matar, S. F. Electronic density of states, 1*s* core-level shifts, and core ionization energies of graphite, diamond, C_3N_4 phases, and graphitic C_11N_4. *Phys. Rev. B* **1999**, *60*, 10855–10863.

(44) Ma, X.; Lv, Y.; Xu, J.; Liu, Y.; Zhang, R.; Zhu, Y. A Strategy of Enhancing the Photoactivity of g-C3N4 via Doping of Nonmetal Elements: A First-Principles Study. *J. Mater. Chem. C* **2012**, *116*, 23485–23493.

(45) Li, F.; Qu, Y.; Zhao, M. Efficient helium separation of graphitic carbon nitride membrane. *Carbon* **2015**, *95*, 51 – 57.

(46) Abdullahi, Y. Z.; Yoon, T. L.; Halim, M. M.; Hashim, M. R.; Lim, T. L. First-principles investigation of graphitic carbon nitride monolayer with embedded Fe atom. *Surf. Sci.* **2018**, *667*, 112–120.

(47) Bafekry, A.; Stampfl, C.; Ghergherehchi, M.; Shayesteh, S. F. A first-principles study of the effects of atom impurities, defects, strain, electric field and layer thickness on the electronic and magnetic properties of the C2N nanosheet. *Carbon* **2020**, *157*, 371 – 384.

(48) Akgenc, B. Intriguing of two-dimensional Janus surface-functionalized MXenes: An ab initio calculation. *Comput. Mater. Sci.* **2020**, *171*, 109231.

(49) Kahraman, Z.; Kandemir, A.; Yagmurcukardes, M.; Sahin, H. Single-layer Janus-type platinum dichalcogenides and their heterostructures. *J. Phys. Chem. C* **2019**, *123*, 4549–4557.

(50) Bafekry, A.; Stampfl, C.; Shayesteh, s. A first-principles study of C3N nanostructures:

View Article Online
DOI: 10.1039/D0CP00093K

Control and engineering of the electronic and magnetic properties of nanosheets, tubes and ribbons. *ChemPhysChem 21*, 164.

(51) Mortazavi, B.; Shahrokhi, M.; Madjet, M. E.; Hussain, T.; Zhuang, X.; Rabczuk, T. N-, B-, P-, Al-, As-, and Ga-graphdiyne/graphyne lattices: first-principles investigation of mechanical, optical and electronic properties. *J. Mater. Chem. C* **2019**, *7*, 3025–3036.

(52) Akgenc, B. New predicted two-dimensional MXenes and their structural, electronic and lattice dynamical properties. *Solid State Communications* **2019**, *303-304*, 113739.

(53) Bafekry, A.; Akgenc, B.; Shayesteh, S. F.; Mortazavi, B. Tunable electronic and magnetic properties of graphene/carbon-nitride van der Waals heterostructures. *Appl. Surf. Sci.* **2020**, *505*, 144450.

(54) Mortazavi, B.; Madjet, M. E.; Shahrokhi, M.; Ahzi, S.; Zhuang, X.; Rabczuk, T. Nanoporous graphene: A 2D semiconductor with anisotropic mechanical, optical and thermal conduction properties. *Carbon* **2019**, *147*, 377 – 384.

(55) Yagmurcukardes, M.; Ozen, S.; Iyikanat, F.; Peeters, F.; Sahin, H. Raman fingerprint of stacking order in HfS 2- Ca (OH) 2 heterobilayer. *Physical Review B* **2019**, *99*, 205405.

(56) Bafekry, A.; Stampfl, C.; Shayesteh, S. F.; Peeters, F. M. Exploiting the Novel Electronic and Magnetic Structure of C3N via Functionalization and Conformation. *Adv. Elect. Mater.* **2019**, *5*, 1900459.

(57) Kiymaz, D.; Yagmurcukardes, M.; Tomak, A.; Sahin, H.; Senger, R. T.; Peeters, F. M.; Zareie, H. M.; Zafer, C. Controlled growth mechanism of poly (3-hexylthiophene) nanowires. *Nanotechnology* **2016**, *27*, 455604.

View Article Online
DOI: 10.1039/D0CP00093K

(58) Akgenc, B. Two-dimensional black arsenic for Li-ion battery applications: a DFT study. *Journal of Materials Science* **2019**, *54*, 9543–9552.

(59) Mortazavi, B.; Shahrokhi, M.; Zhuang, X.; Rabczuk, T. BoronâĂŞgraphdiyne: a superstretchable semiconductor with low thermal conductivity and ultrahigh capacity for Li, Na and Ca ion storage. *J. Mater. Chem. A* **2018**, *6*, 11022–11036.

(60) Bafekry, A.; Farjami Shayesteh, S.; Ghergherehchi, M.; Peeters, F. M. Tuning the bandgap and introducing magnetism into monolayer BC3 by strain/defect engineering and adatom/molecule adsorption. *J. Appl. Phys.* **2019**, *126*, 144304.

(61) Akgenc, B.; Kinaci, A.; Tasseven, C.; Cagin, T. First-principles calculations on stability and mechanical properties of various ABO3 and their alloys. *Mater. Chemistry and Physics* **2018**, *205*, 315 – 324.

(62) Mortazavi, B.; Makaremi, M.; Shahrokhi, M.; Fan, Z.; Rabczuk, T. N-graphdiyne two-dimensional nanomaterials: Semiconductors with low thermal conductivity and high stretchability. *Carbon* **2018**, *137*, 57 – 67.

(63) Ersan, F.; Arslanalp, O.; Gokoglu, G.; Akturk, E. Effect of adatoms and molecules on the physical properties of platinum-doped and -substituted silicene: A first-principles investigation. *Appl. Surf. Sci.* **2016**, *371*, 314 – 321.

(64) Bafekry, A.; Mortazavi, B.; Shayesteh, S. F. Band gap and magnetism engineering in Dirac half-metallic Na2C nanosheet via layer thickness, strain and point defects. *J. Magnetism and Magnetic Materials* **2019**, *491*, 165565.

(65) Bafekry, A.; Shayesteh, S. F.; Peeters, F. M. Introducing novel electronic and magnetic properties in C3N nanosheets by defect engineering and atom substitution. *Phys. Chem. Chem. Phys.* **2019**, *21*, 21070–21083.

View Article Online
DOI: 10.1039/D0CP00093K

(66) Ersan, F.; Gokoglu, G.; Akturk, E. Electronic structure of BSb defective monolayers and nanoribbons. *J. Phys.: Condensed Matter* **2014**, *26*, 325303.

(67) Chan, K. T.; Neaton, J. B.; Cohen, M. L. First-principles study of metal adatom adsorption on graphene. *Phys. Rev. B* **2008**, *77*, 235430.

(68) Bafekry, A.; Ghergherehchi, M.; Shayesteh, S. F. Tuning the electronic and magnetic properties of antimonene nanosheets via point defects and external fields: first-principles calculations. *Phys. Chem. Chem. Phys.* **2019**, *21*, 10552–10566.

(69) Mortazavi, B.; Shahrokhi, M.; Madjet, M. E.; Makaremi, M.; Ahzi, S.; Rabczuk, T. N-, P-, As-triphenylene-graphdiyne: Strong and stable 2D semiconductors with outstanding capacities as anodes for Li-ion batteries. *Carbon* **2019**, *141*, 291 – 303.

(70) Ersan, F.; Arkin, H.; Akturk, E. The effect of vacancies and the substitution of p-block atoms on single-layer buckled germanium selenide. *RSC Adv.* **2017**, *7*, 37815–37822.

(71) Bafekry, A.; Ghergherehchi, M.; Shayesteh, S. F.; Peeters, F. Adsorption of molecules on C3N nanosheet: A first-principles calculations. *Chem. Phys.* **2019**, *526*, 110442.

(72) Tagani, M. B. Semi-hydrogenated polyaniline sheet: A half-metal with exotic properties. *J. Magnetism and Magnetic Materials* **2020**, *497*, 166027.

(73) Bafekry, A.; Shayesteh, S. F.; Peeters, F. C3N Monolayer: Exploring the Emerging of Novel Electronic and Magnetic Properties with Adatom Adsorption, Functionalizations, Electric Field, Charging, and Strain. *J. Phys. Chem. C* **2019**, *123*, 12485–12499.

(74) Tagani, M. B. Electrical and mechanical properties of a fully hydrogenated two-dimensional polyaniline sheet. *Comput. Mater.s Sci.* **2018**, *153*, 126–133.

(75) Bafekry, A.; Shayesteh, S. F.; Peeters, F. M. Two-dimensional carbon nitride (2DCN) nanosheets: Tuning of novel electronic and magnetic properties by hydrogenation, atom substitution and defect engineering. *J. Appl. Phys.* **2019**, *126*, 215104.

View Article Online
DOI: 10.1039/D0CP00093K

(76) Sahin, H.; Peeters, F. M. Adsorption of alkali, alkaline-earth, and 3*d* transition metal atoms on silicene. *Phys. Rev. B* **2013**, *87*, 085423.

(77) Bafekry, A. Graphene-like BC6N single-layer: Tunable electronic and magnetic properties via thickness, gating, topological defects, and adatom/molecule. *Physica E: Low-dimensional Systems and Nanostructures* **2020**, *118*, 113850.

(78) Peljhan, S.; Kokalj, A. Adsorption of Chlorine on Cu(111): A Density-Functional Theory Study. *J. Phys. Chem. C* **2009**, *113*, 14363–14376.

(79) Tagani, M. B.; Vishkayi, S. I. Polyaniline (C3N) nanoribbons: Magnetic metal, semiconductor, and half-metal. *J. Appl. Phys.* **2018**, *124*, 084304.

(80) Bafekry, A.; Stampfl, C.; Peeters, F. Dirac half-metallicity of Thin PdCl3 Nanosheets: Investigation of the Effects of External Fields, Surface Adsorption and Defect Engineering on the Electronic and Magnetic Properties. *Sci. Rep.* **2020**, *10*, 213.

(81) Dong, M. M.; He, C.; Zhang, W. X. A tunable and sizable bandgap of a g-C3N4/graphene/g-C3N4 sandwich heterostructure: a van der Waals density functional study. *J. Mater. Chem. C* **2017**, *5*, 3830–3837.

(82) Yagmurcukardes, M.; Bacaksiz, C.; Senger, R. T.; Sahin, H. Hydrogen-induced structural transition in single layer ReS2. *2D Mater.* **2017**, *4*, 035013.

(83) Bafekry, A.; Stampfl, C.; Akgenc, B.; Ghergherehchi, M. Control of C3N4 and C4N3 carbon nitride nanosheets' electronic and magnetic properties through embedded atoms. *Phys. Chem. Chem. Phys.* **2020**, *22*, 2249–2261.

(84) Yagmurcukardes, M. Monolayer fluoro-InSe: Formation of a thin monolayer via fluorination of InSe. *Phys. Rev. B* **2019**, *100*, 024108.

(85) A. Bafekry, M. N.-A. Tuning the electronic properties of graphene-graphitic carbon

View Article Online
DOI: 10.1039/D0CP00093K

nitride heterostructures and heterojunctions by using an electric field. *Phys. Rev. B* **2020**,

(86) Garg, P.; Choudhuri, I.; Pathak, B. Stanene based gas sensors: effect of spin-orbit coupling. *Phys. Chem. Chem. Phys.* **2017**, *19*, 31325–31334.

(87) Perdew, J. P.; Burke, K.; Ernzerhof, M. Generalized Gradient Approximation Made Simple. *Phys. Rev. Lett.* **1996**, *77*, 3865–3868.

(88) Troullier, N.; Martins, J. L. Efficient pseudopotentials for plane-wave calculations. *Phys. Rev. B* **1991**, *43*, 1993–2006.

(89) Ozaki, T. Variationally optimized atomic orbitals for large-scale electronic structures. *Phys. Rev. B* **2003**, *67*, 155108.

(90) Ozaki, T.; Kino, H. Numerical atomic basis orbitals from H to Kr. *Phys. Rev. B* **2004**, *69*, 195113.

(91) Monkhorst, H. J.; Pack, J. D. Special points for Brillouin-zone integrations. *Phys. Rev. B* **1976**, *13*, 5188–5192.

(92) Tersoff, J.; Hamann, D. R. Theory and Application for the Scanning Tunneling Microscope. *Phys. Rev. Lett.* **1983**, *50*, 1998–2001.

(93) Horcas, I.; Fernandez, R.; Gomez-Rodriguez, J. M.; Colchero, J.; Gomez-Herrero, J.; Baro, A. M. WSXM: A software for scanning probe microscopy and a tool for nanotechnology. *Review of Scientific Instruments* **2007**, *78*, 013705.

(94) Mulliken, R. S. Electronic Population Analysis on LCAO-MO Molecular Wave Functions. IV. Bonding and Antibonding in LCAO and Valence-Bond Theories. *J. Chem. Phys.* **1955**, *23*, 2343–2346.

(95) Wang Xinchen,; Maeda Kazuhiko,; Thomas Arne,; Takanabe Kazuhiro,; Xin Gang,; Carlsson Johan M.,; Domen Kazunari,; Antonietti Markus, A metal-free polymeric

View Article Online
DOI: 10.1039/D0CP00093K

photocatalyst for hydrogen production from water under visible light. *Nature Materials* **2008**, *8*, 76.

(96) Liu, G.; Niu, P.; Sun, C.; Smith, S. C.; Chen, Z.; Lu, G. Q. M.; Cheng, H.-M. Unique Electronic Structure Induced High Photoreactivity of Sulfur-Doped Graphitic C_3N_4. *Journal of the American Chemical Society* **2010**, *132*, 11642–11648.

(97) Srinivasu, K.; Modak, B.; Ghosh, S. K. Porous Graphitic Carbon Nitride: A Possible Metal-free Photocatalyst for Water Splitting. *The Journal of Physical Chemistry C* **2014**, *118*, 26479–26484.

(98) Li, T.; He, C.; Zhang, W. A novel porous C4N4 monolayer as a potential anchoring material for lithium-sulfur battery design. *J. Mater. Chem. A* **2019**, *7*, 4134–4144.

(99) SARIKURT, S.; ERSAN, F. Phononic Stability Analysis of Two-Dimensional Carbon Nitride Monolayers. *Marmara Fen Bilimleri Dergisi* **2018**, *30*, 383 – 387.

(100) Wirth, J.; Neumann, R.; Antonietti, M.; Saalfrank, P. Adsorption and photocatalytic splitting of water on graphitic carbon nitride: a combined first principles and semiempirical study. *Phys. Chem. Chem. Phys.* **2014**, *16*, 15917–15926.

(101) Li, X.; Dai, Y.; Ma, Y.; Han, S.; Huang, B. Graphene/g-C_3N_4 bilayer: considerable band gap opening and effective band structure engineering. *Phys. Chem. Chem. Phys.* **2014**, *16*, 4230–4235.

View Article Online
DOI: 10.1039/D0CP00093K

Table 1: The calculated ground-state structural, electronic and magnetic parameters of embedding atom@$C_6N_{6,8}$: bond length between embedded-atom and its nearest neighbor atom (d_{AN}), bond length between C-C atoms (d_{CC}), the bond length between N-C atoms (d_{NC}), the electronic state (ES), as specified as metal (M), half-metal (HM), ferromagnetic-metal (FM), semiconductor (SC), spin-gapless semiconductor (SG-SC) and dilute-magnetic semiconductor (DM-SC), the charge transfer (ΔQ) between embedding atom and $C_6N_{6,8}$, the magnetic moment per supercell $M_{tot}(\mu_B)$, and the initial magnetic moment of the atoms $M_{ISO}(\mu_B)$. The values in parentheses are corresponding values for the C_6N_8 monolayer.

Adatom	d_{AN} (Å)	d_{NC} (Å)	d_{CC} (Å)	ES	ΔQ (e)	$M_{tot}(\mu_B)$	$M_{ISO}(\mu_B)$
H	1.038 (1.270)	1.391 (1.387)	1.442	DM-SC (SG-SC)	0.38 (0.30)	1 (0.95)	1
O	1.263 (1.293)	1.439 (1.427)	1.447	DM-SC (SC)	-0.33 (-0.41)	3.8 (0)	2
S	1.828 (1.870)	1.435 (1.429)	1.420	SC (SC)	0.10 (-0.38)	0 (0)	2
F	1.488 (1.908)	1.418 (1.375)	1.465	DM-SC (DM-SC)	-0.24 (-0.13)	1 (1)	1
Cl	1.742 (2.180)	1.405 (1.408)	1.451	DM-SC (HM)	0.06 (0.90)	1.06 (1.3)	1
B	1.445 (1.441)	1.441 (1.455)	1.449	DM-SC (DM-SC)	0.45 (0.42)	0.95 (1)	1
C	1.463 (1.396)	1.439 (1.446)	1.469	SC (SC)	0.40 (0.42)	0 (0)	2
Si	1.936 (1.926)	1.417 (1.411)	1.452	SC (FM)	0.63 (1.24)	0 (0.3)	2
N	1.465 (1.441)	1.456 (1.422)	1.449	DM-SC (HM)	0.06 (0.02)	1 (0.63)	3
P	1.836 (1.868)	1.438 (1.414)	1.433	DM-SC (HM)	0.21 (0.48)	0.9 (0.70)	3
Li	2.138 (2.070)	1.372 (1.366)	1.459	M (HM)	0.61 (0.82)	0 (0.95)	1
Na	2.674 (2.389)	1.365 (1.361)	1.461	M (HM)	0.61 (0.57)	0 (0.95)	1
K	2.721 (2.429)	1.363 (1.351)	1.466	SC (HM)	0.68 (0.75)	0 (0.95)	1
Be	1.626 (1.441)	1.408 (1.455)	1.448	SC (SC)	0.68 (0.78)	0 (0)	0
Mg	2.163 (2.304)	1.390 (1.416)	1.443	SC (M)	0.99 (1.38)	0 (0)	0
Ca	2.668 (2.376)	1.380 (1.381)	1.449	M (FM)	1.17 (1.32)	0.0 (1)	0
Al	1.955 (2.016)	1.407 (1.420)	1.440	DM-SC (SG-SC)	0.78 (0.8)	1(0.85)	1
Sc	2.200 (2.332)	1.416 (1.404)	1.426	HM (M)	1.18 (1.20)	0.8 (0)	1
Ti	2.065 (2.320)	1.421 (1.404)	1.416	SG-SC (FM)	0.80 (0.77)	1.9 (1.6)	2
V	1.968 (2.309)	1.420 (1.403)	1.420	SG-SC (HM)	0.66 (0.62)	2.76 (1)	3
Cr	1.941 (2.167)	1.415 (1.406)	1.427	FM (HM)	0.56 (0.63)	2.4 (2.1)	4
Mn	1.853 (1.995)	1.412 (1.408)	1.425	HM (HM)	1.26 (1.27)	3 (3.2)	5
Fe	1.855 (1.808)	1.409 (1.397)	1.433	DM-SC (FM)	0.67 (0.74)	2 (1.7)	4
Co	1.869 (1.891)	1.399 (1.424)	1.438	SG-SC (FM)	0.56 (0.51)	0.95 (0.8)	3
Ni	1.983 (2.008)	1.391 (1.401)	1.449	SC (HM)	0.59 (0.58)	0 (2)	2
Cu	2.066 (2.227)	1.374 (1.375)	1.457	FM (SG-SC)	0.47 (0.40)	0.5 (0.72)	1
Zn	2.049 (2.335)	1.384 (1.398)	1.442	SC (SC)	0.74 (0.67)	0 (0)	0

View Article Online
DOI: 10.1039/D0CP00093K

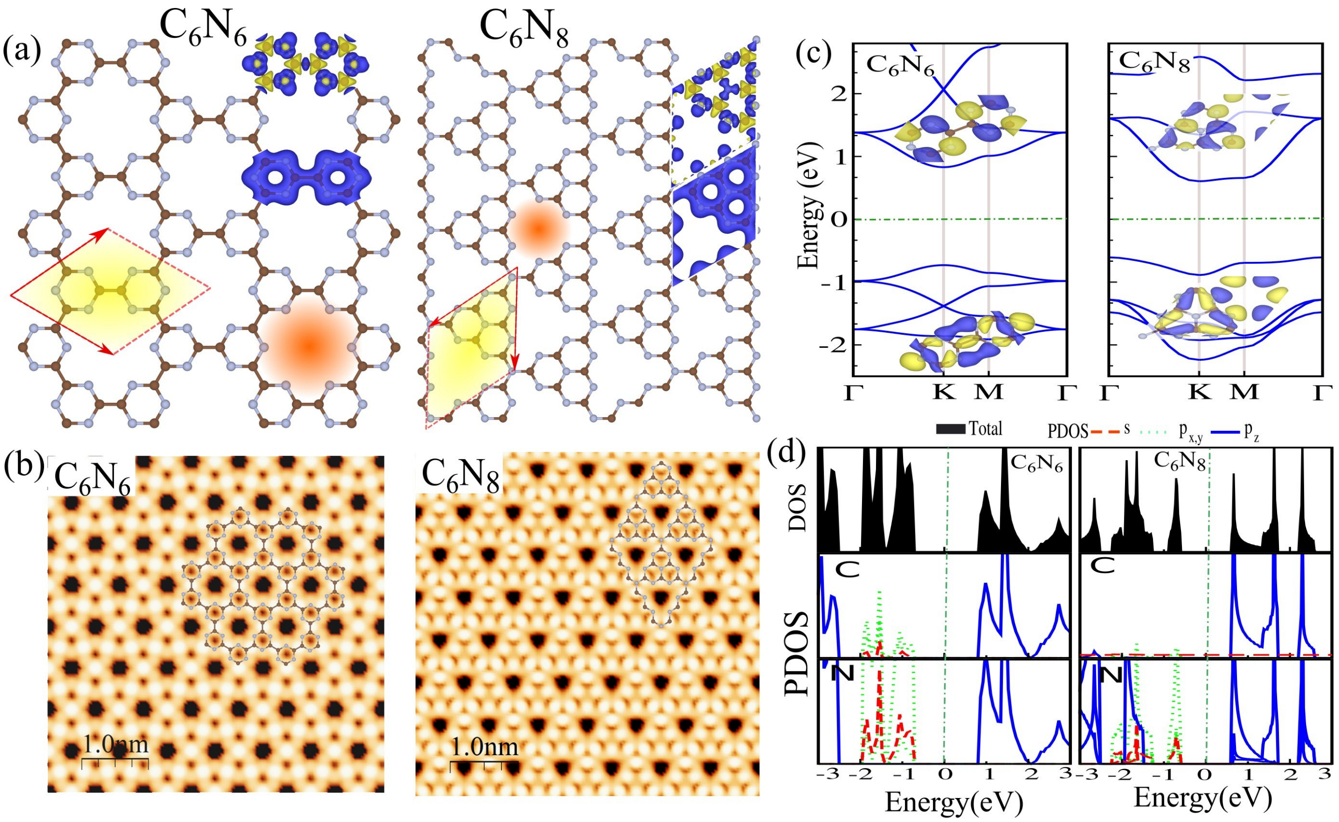

Figure 1: (a) Atomic structures, (b) simulated STM images, (c) electronic band structure, and (d) DOS and PDOS of C_6N_6 and C_6N_8 monolayers. The primitive unit cell is indicated by a red parallelogram in (a). C and N atoms represent by brown and blue balls, respectively. Total charge density and charge difference density are also analyzed. The charge accumulation and depletion are shown by color scheme with blue and yellow regions, respectively. The STM images are overlayed with the atomic structures. The charge densities of the valance band maximum (VBM) and conduction band minimum (CBM) are indicated in the insets. Fermi level (E_F) is set to zero.

View Article Online
DOI: 10.1039/D0CP00093K

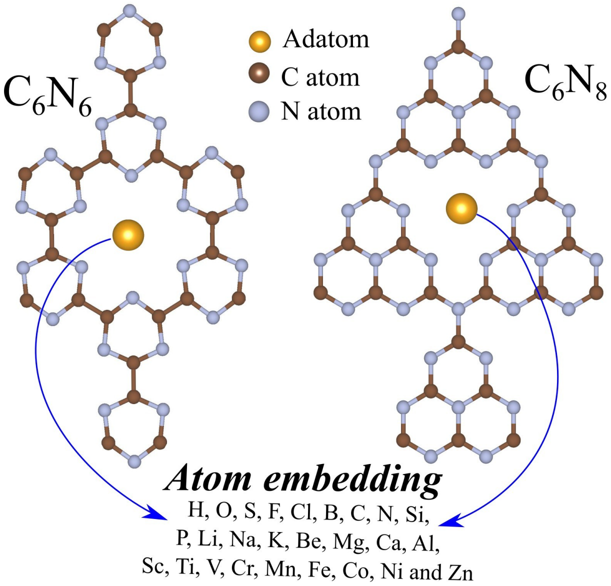

Figure 2: Schematic atomic structure for the embedding of atoms into the holey site of C_6N_6(left) and C_6N_8(right) monolayers.

View Article Online
DOI: 10.1039/D0CP00093K

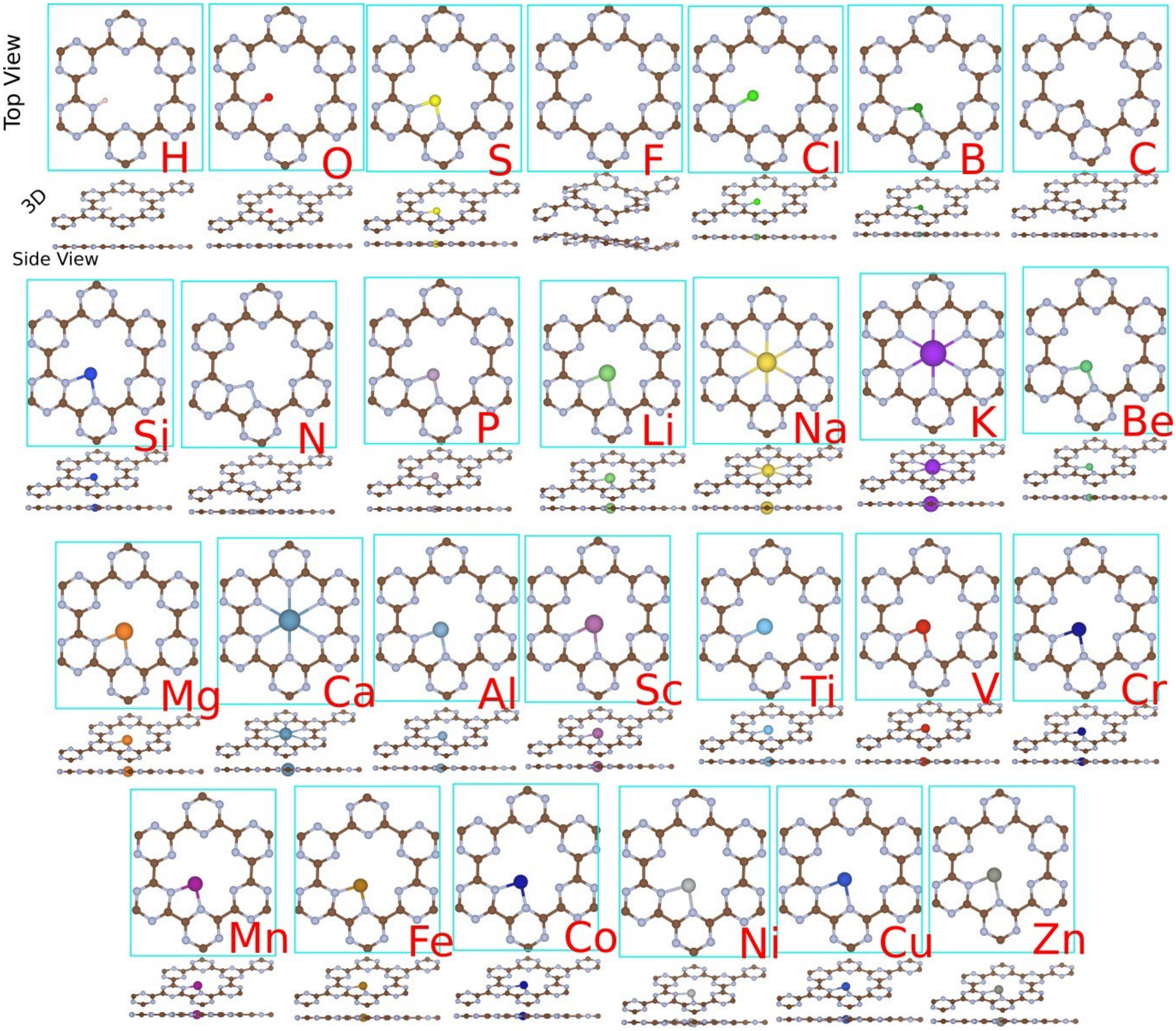

Figure 3: Top, perspective and side views of the optimized structures of different atoms embedded into the holey site of the C_6N_6 monolayer.

View Article Online
DOI: 10.1039/D0CP00093K

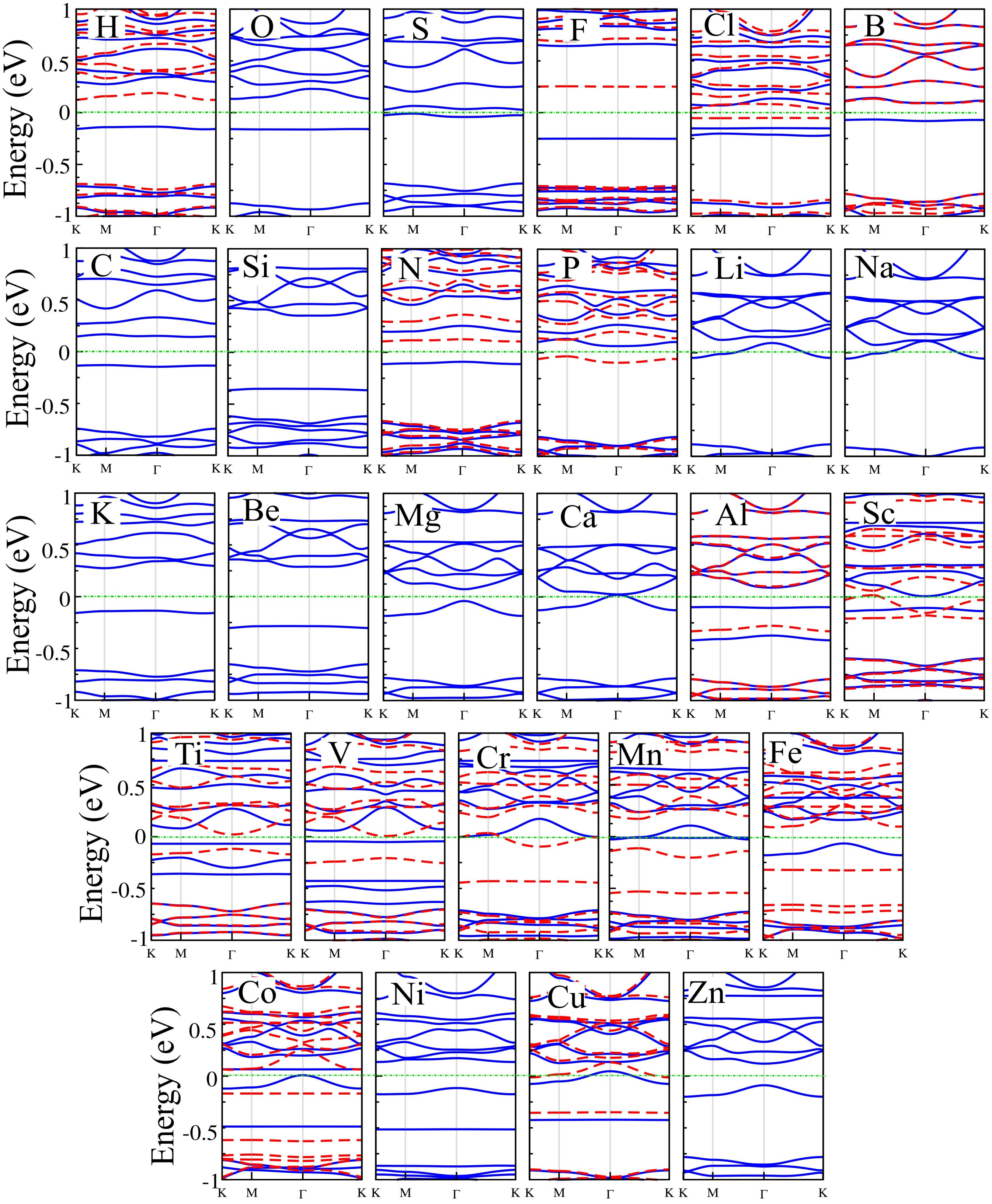

Figure 4: Electronic structure of different atoms embedded into the holey site of C_6N_6. Fermi level E_F is set to zero.

View Article Online
DOI: 10.1039/D0CP00093K

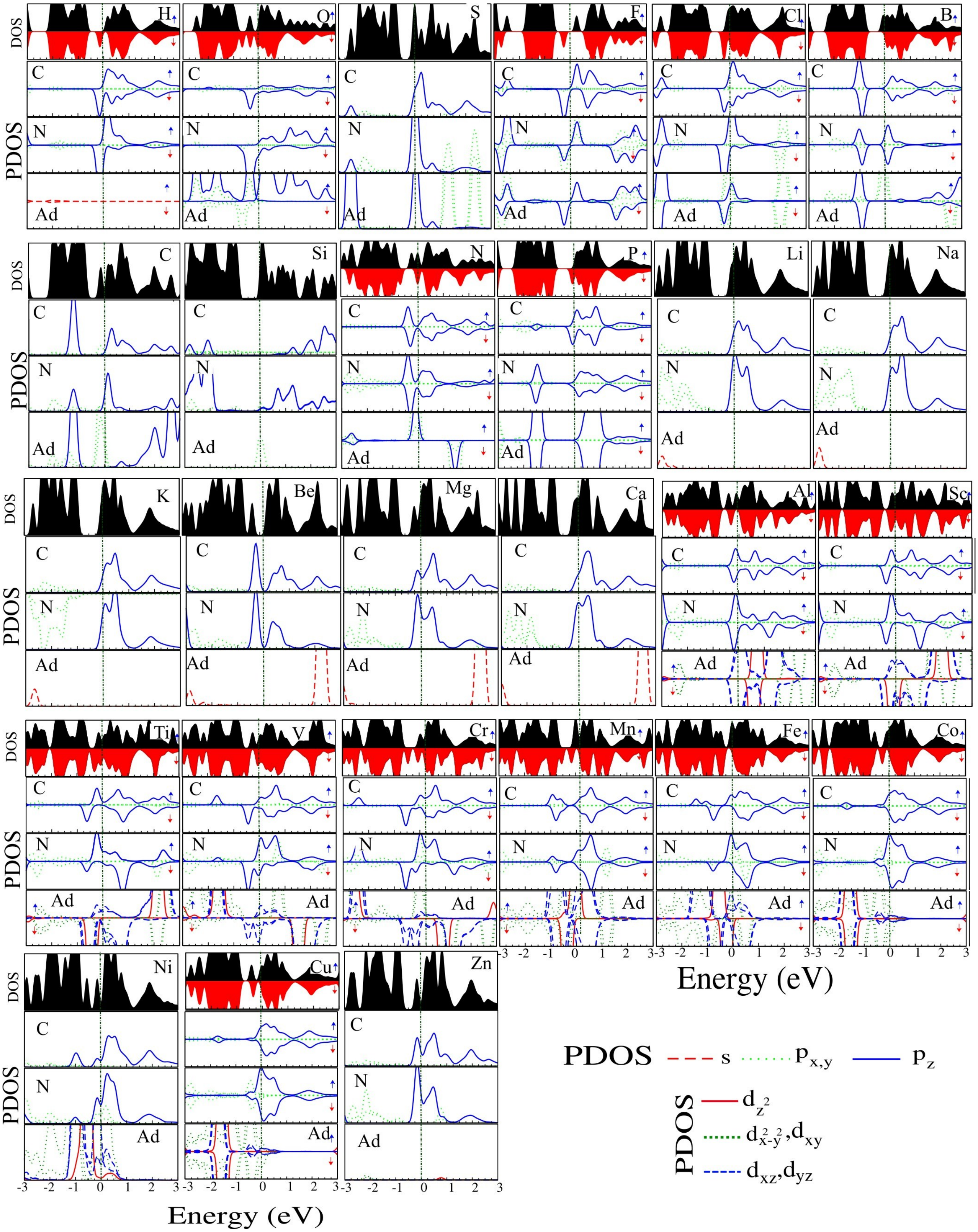

Figure 5: DOS and PDOS of different atoms embedded into the holey site of the C_6N_6 monolayer. The zero of energy is set at E_F.

View Article Online
DOI: 10.1039/D0CP00093K

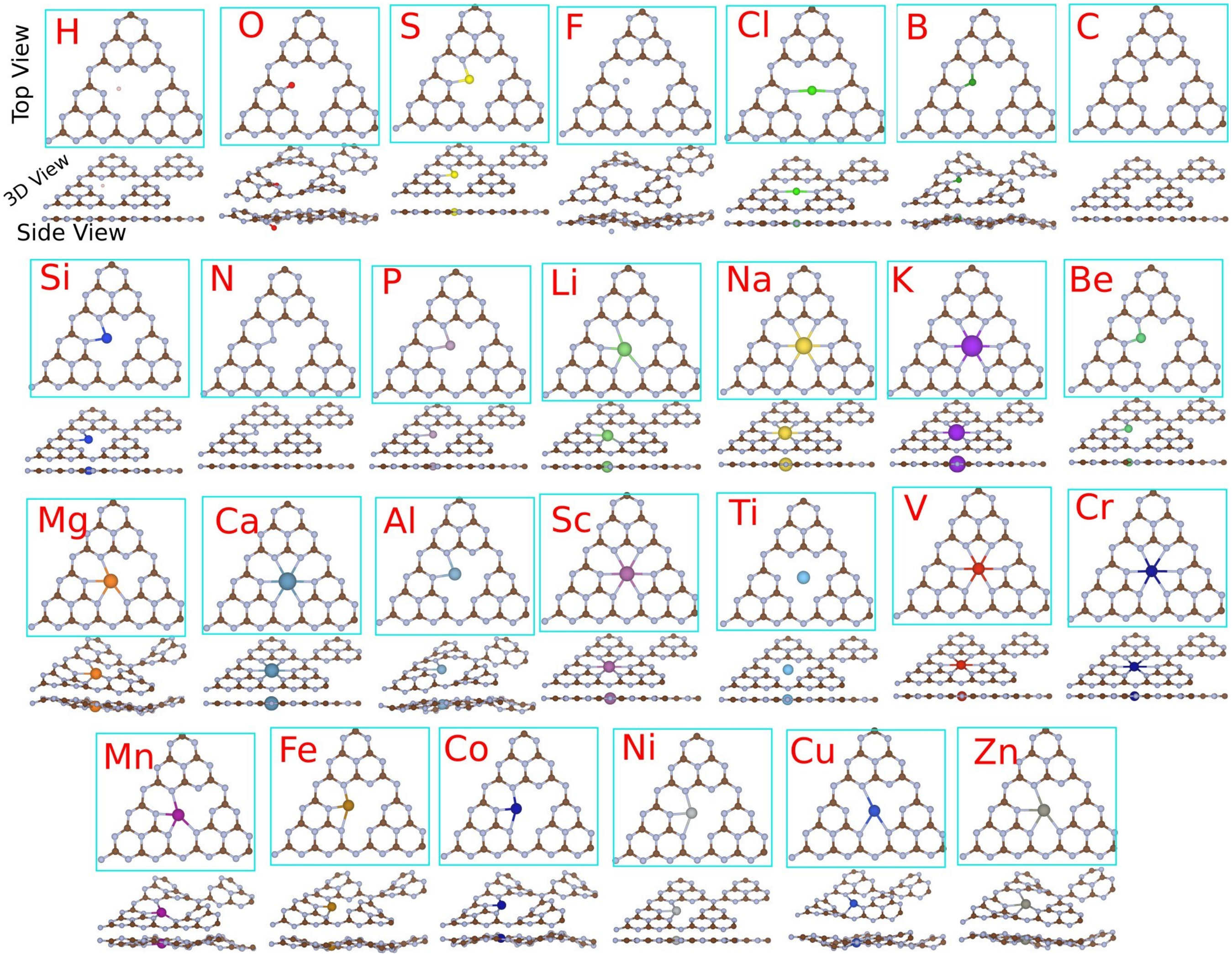

Figure 6: Top, perspective and side views of the optimized structures of different atoms embedded into the holey site of the C_6N_8 monolayer.

View Article Online
DOI: 10.1039/D0CP00093K

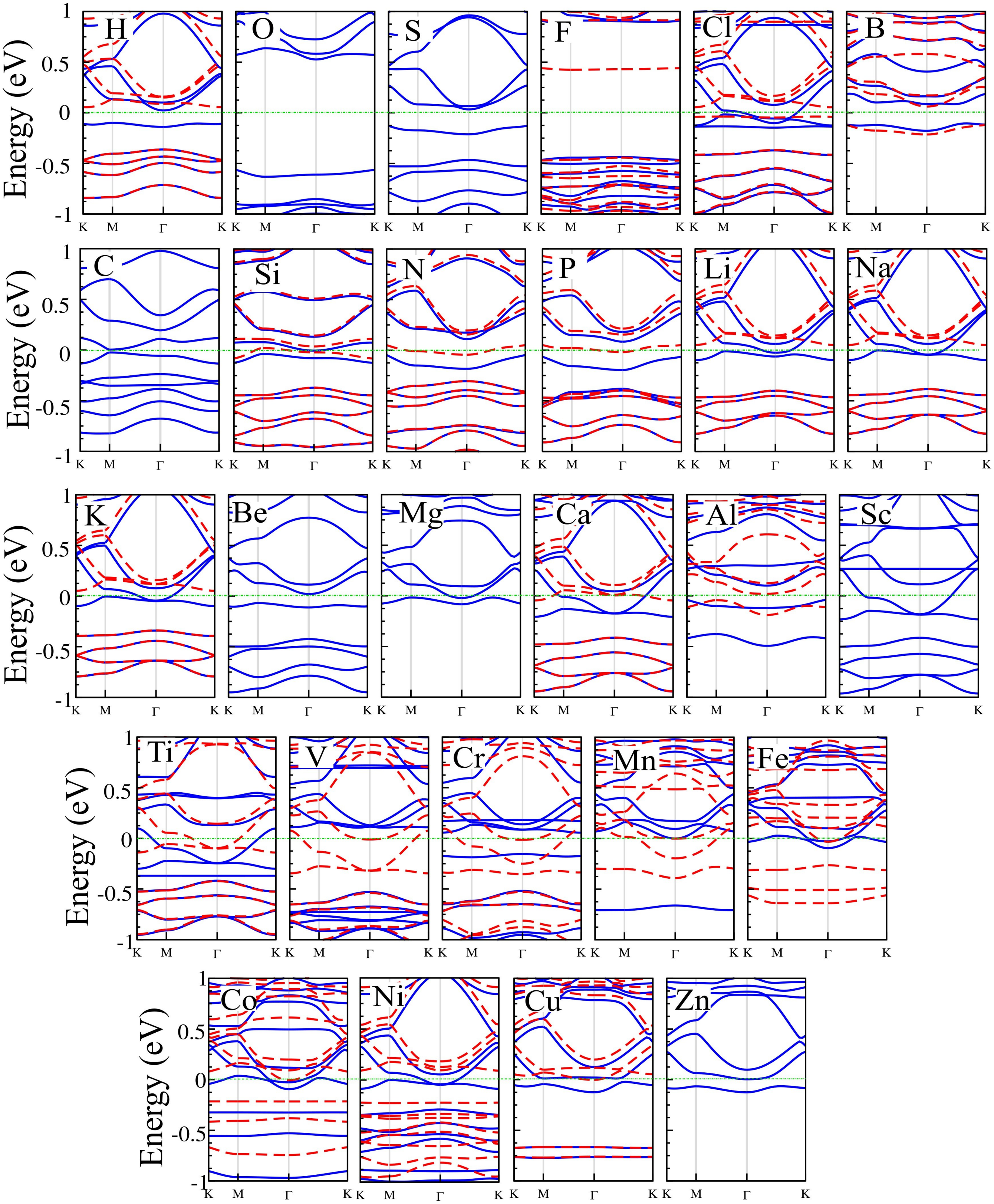

Figure 7: Electronic structure of different atoms embedded into the holey site of the C_6N_8 monolayer. Fermi level E_F is set to zero.

View Article Online
DOI: 10.1039/D0CP00093K

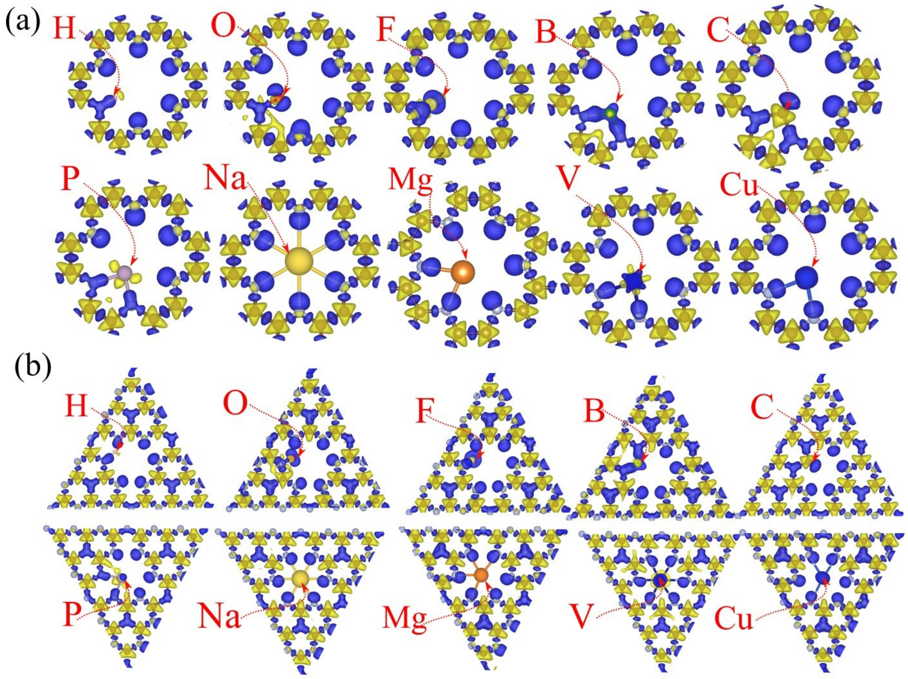

Figure 8: Difference charge density of different atoms embedded into the holey site of (a) C_6N_6 and (b) C_6N_8 monolayers. The charge accumulation and depletion are shown by color scheme with blue and yellow regions, respectively.

View Article Online
DOI: 10.1039/D0CP00093K

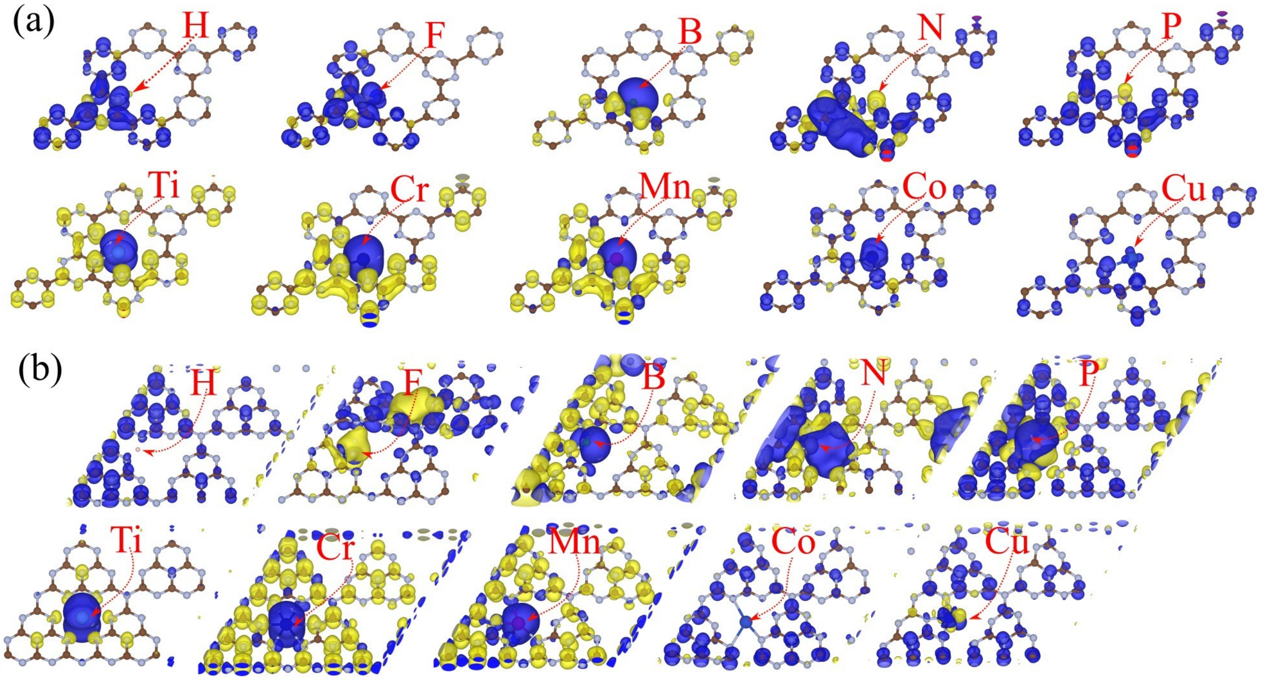

Figure 9: Difference spin density of different atoms embedded into the holey site of (a) C_6N_6 and (b) C_6N_8 monolayers. The blue and yellow regions represent the ↑ and ↓ spin states, respectively.

View Article Online
DOI: 10.1039/D0CP00093K

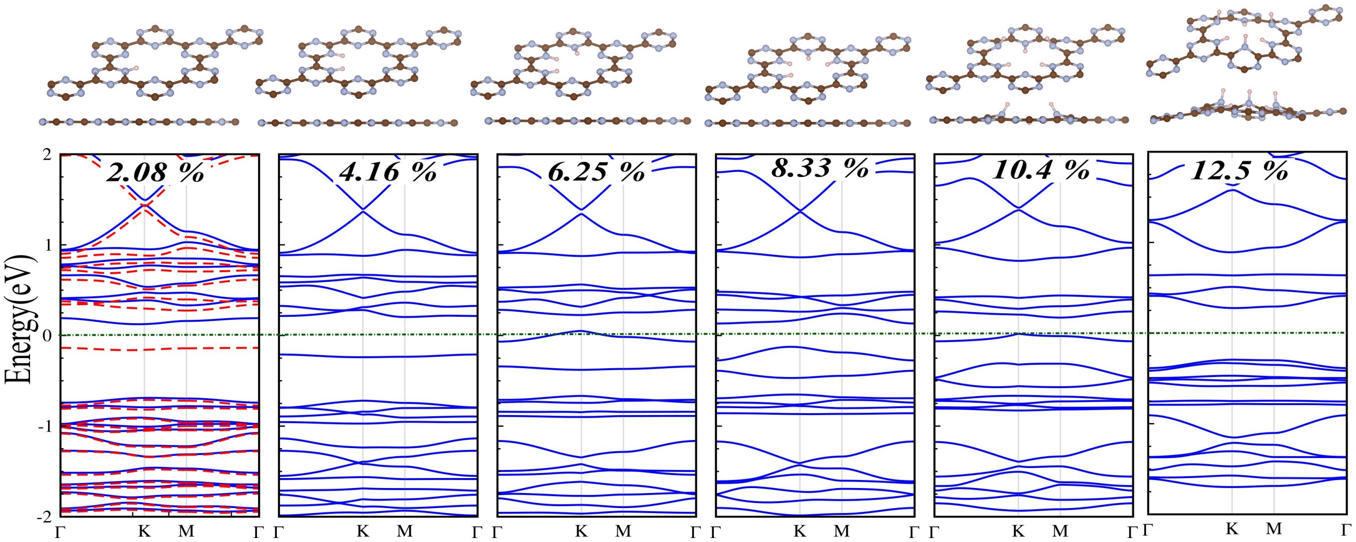

Figure 10: Electronic band structure of H-embedded into the holey site of the C_6N_6 monolayer as a function of the H atom concentrations. Fermi level E_F is set to zero. The optimized atomic structures is show in top panel.

View Article Online
DOI: 10.1039/D0CP00093K

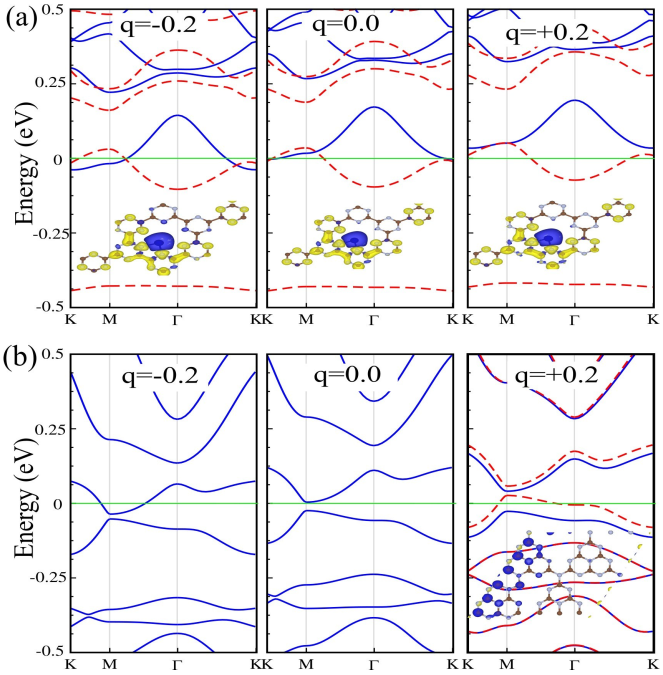

Figure 11: Electronic structure of (a) Cr-embedded C_6N_6 and (b) C-embedded C_6N_8 as a function of the applied charging. The q>0 e and q<0 e, corresponds to the loss or gain of one electron the C_6N_6, are respectively. Fermi level E_F is set to zero.

View Article Online
DOI: 10.1039/D0CP00093K

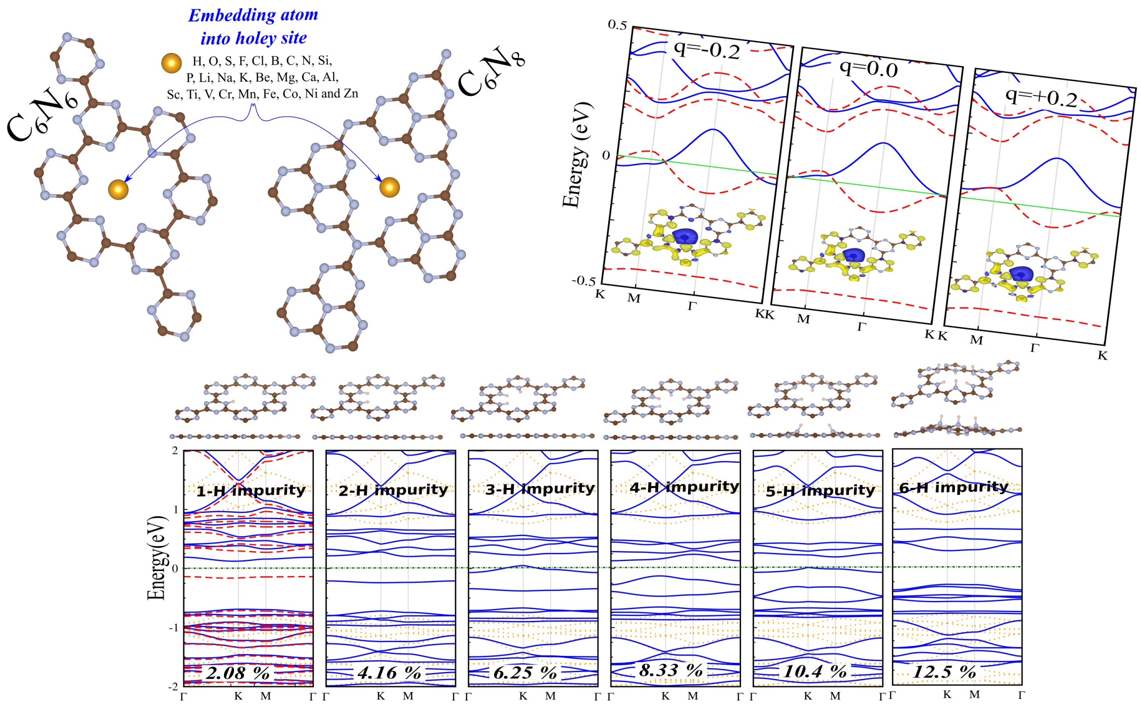

TOC